



## Enhancing piezoelectric energy harvesters with rotating triangular auxetic structures

Xiaofan Zhang, Xiaobiao Shan<sup>\*</sup>, Guangdong Sui, Chengwei Hou, Xuteng Du, Zhaowei Min, Tao Xie

*State Key Laboratory of Robotics and System, Harbin Institute of Technology, Harbin 150001, China*



### ARTICLE INFO

**Keywords:**  
 Auxetic  
 Mechanical metamaterials  
 Piezoelectric energy harvester  
 Enhanced performance  
 Low-frequency environmental vibration energy  
 Rotating triangular structure

### ABSTRACT

The development of piezoelectric energy harvesters is currently constrained by factors such as output power, bandwidth, and natural frequency, which limit their capacity to efficiently capture the low-frequency vibrational energy prevalent in the environment. To address these challenges, this paper proposes a novel approach to enhance the performance of piezoelectric energy harvesters by integrating a rotating triangular auxetic structure. A method for analyzing the mechanical performance of the auxetic structure under lateral constraints is introduced, demonstrating that the structure exhibits favorable negative Poisson's ratio characteristics and design flexibility. Furthermore, the auxetic structure is incorporated into a cantilever beam piezoelectric energy harvester to design and fabricate a novel auxetic-enhanced energy harvester (AEH), alongside a plate substrate energy harvester (PEH) for comparison. Finite element method (FEM) simulations and experimental results show that the auxetic structure increases the average stress in the piezoelectric patch, creating a distinct negative Poisson's ratio region. Under varying geometric parameters and unit cell numbers, the proposed AEH outperforms the conventional PEH, with output power improvements ranging from 96.3 % to 266.1 %, and reductions in natural frequency between 15.35 % and 42.65 %. By appropriately selecting geometric parameters, the AEH also broadens the energy harvesting bandwidth. This enhancement makes the AEH particularly well-suited for capturing low-frequency vibrational energy from the environment. The large negative Poisson's ratio of the auxetic structure, as demonstrated in this study, contributes to an increased energy density in the piezoelectric patch.

### 1. Introduction

As microelectronic systems and the Internet of Things continue to evolve, wireless sensors have become increasingly important in monitoring environmental conditions and machine operations [1]. Currently, these sensors are typically powered by chemical batteries, which have limitations such as short lifespans and difficulty in replacement, hindering the further advancement of wireless sensor technology [2]. A promising solution to these challenges is the harvesting of vibration energy from the environment to power low-power wireless sensors, thereby achieving energy self-sufficiency [3]. Vibrational energy is a ubiquitous energy source in daily life [4], derived from various origins such as machinery [5], vehicles [6], bridges [7], human activities [8], wind [9], and tidal forces [10]. Researchers have primarily focused on piezoelectric [11], electromagnetic [12], and triboelectric [13] methods for converting vibration energy into electrical energy [14]. Of these,

piezoelectric energy harvesters are widely researched and applied due to their high energy density, ease of miniaturization, and simple structure [15].

The rectangular cantilever beam piezoelectric energy harvester is a typical solution for energy harvesting [16]. It features a simple structure and broad applicability [17], capable of generating electrical energy at the micro-watt to milli-watt scale when the excitation frequency of environmental vibrations aligns with its natural frequency [18]. However, this type of harvester often suffers from a narrow bandwidth [19], and its high natural frequency renders it ineffective in capturing the low-frequency vibrations commonly present in the environment [20]. Additionally, the low output power significantly limits its broader application [21]. To address these issues, researchers have explored various strategies to optimize the performance of piezoelectric energy harvesters, including the introduction of multistable mechanical structures [22], the development of multi-degree-of-freedom systems [23],

\* Corresponding author.

E-mail address: [shanaxiaobiao@hit.edu.cn](mailto:shanaxiaobiao@hit.edu.cn) (X. Shan).

and the enhancement of piezoelectric transducer geometries [24]. Leveraging mechanical nonlinearity and incorporating multistable structures into piezoelectric vibration harvesters are key approaches for broadening operational bandwidth and enhancing the collection of low-frequency vibration energy [25]. Xie et al. [26] designed a multi-modal E-shaped piezoelectric energy harvester with a built-in bistability and internal resonance to collect low-frequency vibration energy. Wang et al. [27] presented a portable, stacked and tri-stable energy harvester based on the nonlinearity of magnetic force to harness low-frequency and low-level excitations. Inspired by the predatory action of the Venus flytrap, Qian et al. [28] designed a low-cost bistable piezoelectric energy harvester capable of broadband energy harvesting within the 9–14 Hz range. Ma et al. [29] examined the nonlinear characteristics and energy harvesting performance of an asymmetric tristable energy harvester, demonstrating that this device can more easily enter interwell motion, effectively capturing low-frequency vibration energy from the environment. Sun et al. [30] proposed a bistable piezoelectric energy harvester with two magnets, which can adapt to different environmental vibration excitations. Mei et al. [31] introduced a quadstable energy harvester with a time-varying potential well, capable of capturing energy from low-frequency rotational motion, thereby providing a suitable power source for wireless sensors in the Internet of Things. Introducing additional structures such as stoppers in piezoelectric energy harvesters can also improve their performance [32]. Lin et al. [33] designed the deformation-restricted piezoelectric vibration energy harvester to utilize the stopper to limit the maximum deformation of the piezoelectric beam, facilitating unidirectional deformation. Zhang et al. [34] designed a pendulous piezoelectric rotational energy harvester through magnetic plucking of a fan-shaped hanging composite plate. Sun et al. [35] utilized the elliptical cylinder interference to enhance piezoelectric energy harvesting. Kan et al. [36] designed a self-excited unibody piezoelectric energy harvester by utilizing rotationally induced pendulation of along-grooved iron balls. Zhang et al. [37] proposed a novel piezoelectric vibration energy harvester by using a wedge cam to limit the maximum deformation of the cantilevered piezoelectric vibrator. Lin et al. [38] designed a pendulum-like deformation-limited piezoelectric vibration energy harvester triggered indirectly via a smoothly plucked drive plate.

Optimizing the geometry of the piezoelectric cantilever beam can enhance the stress distribution on the piezoelectric material and change the vibration modes, resulting in more efficient energy harvesting [39]. Benasciutti et al. [40] conducted studies on trapezoidal piezoelectric cantilever beams, concluding that an inverted trapezoidal beam with a free wide end outputs more energy than a trapezoidal beam with a fixed wide end, and both outperform rectangular beams. Mohamed et al. [41] used FEM simulations to analyze T-shaped, rectangular, L-shaped, trapezoidal, and triangular piezoelectric cantilever beams, finding that the T-shaped beam achieves the highest maximum output power, 3.4 times that of the triangular beam. Piyarathna et al. [42] investigated an arc-shaped branch beam harvester to improve the energy-harvesting capability in ultra-low-frequency applications. Wang et al. [43] designed and analyzed a hollow triangular piezoelectric cantilever energy harvester, discovering that this shape offers a lower resonant frequency and higher power output. Zhang et al. [44] proposed a L-shaped cantilever beam piezoelectric energy harvester with frequency up-conversion for ultra-low speed rotating environments. Arranging multiple piezoelectric energy harvesters in arrays is another key method to enhance performance [45]. Shim et al. [46] developed a nonlinear piezoelectric energy harvester with a coupled beam array, achieving broadband energy harvesting within the 40 Hz to 80 Hz frequency range using four piezoelectric beams with different natural frequencies. Wang et al. [47] designed an array of multiple piezoelectric energy harvesters based on wind-induced vibrations. Dong et al. [48] proposed a piezoelectric buckled beam array on a pacemaker lead for energy harvesting. Na et al. [49] fabricated a Horizontally assembled trapezoidal piezoelectric cantilever beam array driven by magnetic coupling for

rotational energy harvesting applications. Hou et al. [50] established an E-shaped broadband, multi-band piezoelectric energy harvester composed of three piezoelectric beams, which effectively collects energy from rotating machinery at varying speeds.

In recent years, auxetic metamaterials have garnered significant attention from researchers [51]. These materials exhibit counterintuitive deformation behavior, unlike traditional materials with a positive Poisson's ratio, auxetic materials contract laterally when compressed and expand laterally when stretched [52]. Common auxetic metamaterials include re-entrant hexagonal structures [53], rotating polygon structures [54], and chiral structures [55]. These structures typically offer excellent shear resistance [56], indentation resistance [57], fracture resistance [58], co-directional stretching behavior [59], variable permeability [60], and enhanced energy absorption capabilities [61]. Consequently, they have been widely applied in auxetic textiles [62], smart sensors [63], and sound insulators [64]. Notably, this unique mechanical property also improves stress distribution in piezoelectric materials, thereby enhancing the performance of piezoelectric energy harvesters [65]. Chen et al. [66] designed a nonlinear auxetic piezoelectric energy harvester, incorporating two types of auxetic structures laser-cut into a clamped beam. Compared to traditional nonlinear energy harvesters, these designs increased output power by 173 % and 94 %, and enhanced bandwidth by 1556 % and 2142 %, respectively. Ebrahimian et al. [67] developed an auxetic clamped resonator for efficient vibration energy harvesting under low-frequency excitation and proposed three different auxetic structures. Experimental tests showed that, compared to traditional structures, these auxetic designs increased output power by 10, 6.7, and 6.1 times, respectively, while reducing the natural frequency by 30.45 %, 19.55 %, and 27.53 %, making them suitable for low-frequency, displacement-limited conditions. Eghbali et al. [68] introduced an auxetic lattice resonator supported by an acoustic rectangular tube, which amplified the sound pressure level by approximately 10.5 times at 100 dB compared to traditional cantilever resonators, significantly improving the performance of acoustic energy harvesting systems. Fang et al. [69] proposed a nonlinear vortex-induced vibration energy harvester incorporating an auxetic structure to compensate for the reduction in peak energy output caused by monostable softening due to its negative Poisson's ratio and high-stress distribution. Furthermore, Gao et al. [70] used hierarchical auxetic structure and optimization techniques to enhance the output performance of energy harvesters.

Previous studies have often focused on evaluating energy harvesting performance across various auxetic shapes [71] and geometric parameters [72], with limited attention to the impact of the negative Poisson's ratio on energy harvesting efficiency. Additionally, research has primarily concentrated on a few auxetic structures, such as re-entrant hexagonal configurations [73], while studies on rotating polygonal auxetic structures—known for their exceptional flexibility [74]—have been relatively rare. When integrated into a beam, rotating polygonal auxetic structures experience lateral displacement constraints at the vertices, resulting in mechanical properties that differ significantly from those observed in a freely rotating state—a factor often overlooked in earlier research [75].

This paper proposes a method to enhance the performance of piezoelectric energy harvesting by integrating a rotating triangular auxetic structure. Section 2 presents a numerical solution for the Poisson's ratio behavior of the auxetic structure under lateral displacement constraints on both sides. The impact of geometric parameters and unit cell numbers on the mechanical properties is analyzed, demonstrating that the auxetic structure exhibits favorable negative Poisson's ratio characteristics and design flexibility. In Section 3, the auxetic structure is integrated into a cantilever beam piezoelectric energy harvester, resulting in the design of an auxetic-enhanced energy harvester (AEH) for comparison with a plate substrate energy harvester (PEH). A finite element simulation model is developed, and the results indicate that the auxetic structure significantly increases the average stress on the

piezoelectric patch and creates a distinct negative Poisson's ratio region, thereby enhancing energy harvesting. Section 4 describes the fabrication of prototypes for both AEH and PEH, with experimental results validating the finite element simulations. The effects of various parameters and unit cell numbers on energy harvesting performance are discussed, along with an examination of the relationship between negative Poisson's ratio and piezoelectric energy harvesting efficiency.

## 2. Auxetic structure

This section presents the design of a single-cell rotating triangular auxetic structure, alongside the development of a numerical solution method for its negative Poisson's ratio behavior under lateral displacement constraints on both sides. Additionally, a rotating triangular auxetic structure with multiple unit cells is proposed, and the relationship between the number of constraints and degrees of freedom within the array structure is analyzed. The influence of different constraint relationships on the negative Poisson's ratio performance is also evaluated.

The auxetic structure examined in this paper is the rotating triangular auxetic structure. The fundamental unit cell of this structure comprises four triangles, with adjacent triangles connected by small fan-shaped elements, as shown in Fig. 1. When this structure is machined onto a rectangular beam, the top and bottom triangles are similarly connected to the rectangular plates on both sides by small fan-shaped elements. Given that the radius of these fan-shaped elements is often significantly smaller than the side length of the triangles and the width of the rectangular beam  $W_b$ , the deformation of the rigid parts during the deformation process can be approximately neglected. Consequently, in this study, the fan-shaped elements are treated as flexible hinges, while the remaining components are considered rigid. When the auxetic structure is subjected to longitudinal force, the rigid parts are assumed to remain undeformed, with all deformation occurring in the flexible

hinges [76]. The triangles and rectangular plates rotate about these flexible hinges. For simplicity in analysis, the four triangles are assumed to be identical isosceles triangles with a vertex angle of  $\delta$ , and the angles between the triangles in the undeformed state are all  $\theta$ .

Due to the different angles of the fan-shaped flexible hinges, to ensure similar stiffness among the hinges, a reference hinge radius  $r$  is defined. At this point, the radii of the hinges can be expressed as:

$$\left(\frac{180^\circ - \delta}{2} + \varphi\right)r_1 = \left(\frac{180^\circ + \delta}{2} + \theta\right)r_2 = \left(\frac{180^\circ - \theta}{2}\right)r_3. \quad (1)$$

Since the rigid triangles are assumed to undergo no deformation during the longitudinal deformation process, their side lengths remain unchanged. Therefore, the following relationships hold:

$$\begin{cases} (x_A - x_C)^2 + (y_A - y_C)^2 = m^2 \\ (x_C - x_O)^2 + (y_C - y_O)^2 = n^2 \end{cases}. \quad (2)$$

Based on Eq. (4), the positions of all points during the longitudinal deformation process, along with the changes in length  $X_1'$  and width  $X_2'$ , can be determined. When points A, C, and O align along the same straight line, the structure reaches a fully extended state, and its length attains the maximum value  $X_{2\max}$ . The maximum tensile length  $t_{s\max}$  can be expressed as:

$$t_{s\max} = m\sqrt{\left(1 + 2\sin\frac{\delta}{2}\right)^2 - \left(\sin\frac{\delta}{2}\sin\frac{\theta}{2} + \cos\frac{\delta}{2}\cos\frac{\theta}{2}\right)^2} - 3m\sin\frac{\delta}{2}\cos\frac{\theta}{2} - m\cos\frac{\delta}{2}\sin\frac{\theta}{2}. \quad (3)$$

When points E and G coincide, the structure reaches a fully compressed state, where the angle  $\beta$  becomes zero. At this point, the maximum compressed length  $t_{c\max}$  can be expressed as:

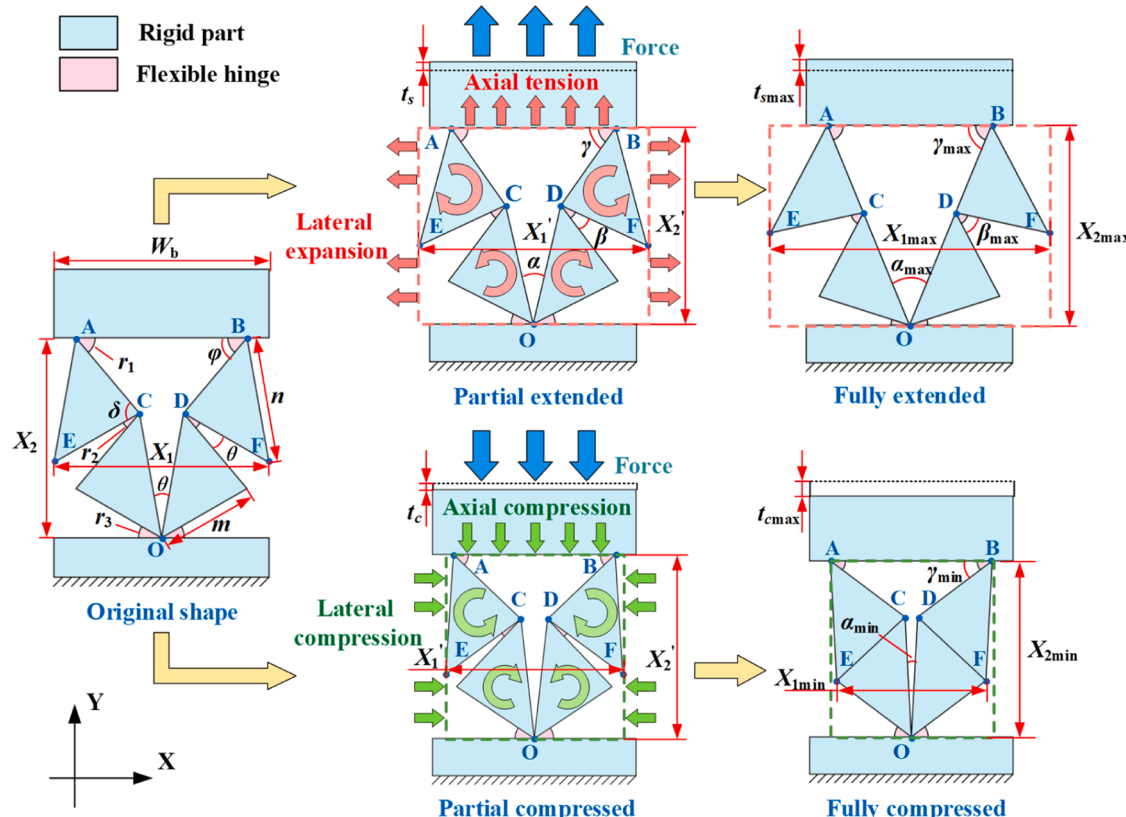


Fig. 1. Rotating triangular auxetic structure.

$$t_{\max} = 3m \sin \frac{\delta}{2} \cos \frac{\theta}{2} + m \cos \frac{\delta}{2} \sin \frac{\theta}{2} - m \sqrt{1 + 8 \sin^2 \left( \frac{\delta}{2} \right) - \left( \sin \frac{\delta}{2} \sin \frac{\theta}{2} + \cos \frac{\delta}{2} \cos \frac{\theta}{2} \right)^2}. \quad (4)$$

During the process of structural longitudinal deformation, the deformation length  $t$  is defined. When  $t$  is positive, the structure undergoes tensile deformation; when  $t$  is negative, the structure is compressed. The deformation length  $t$  must meet the following condition:

$$-t_{\max} \leq t \leq t_{\max}. \quad (5)$$

Additionally, to prevent the structure from being in the fully extended state at the initial position, the geometric dimensions of the structure should satisfy the following relationship:

$$\theta + \frac{\delta}{2} < 90^\circ. \quad (6)$$

The Poisson's ratio of the structure can be expressed as:

$$\nu_{12} = (\nu_{12})^{-1} = -\frac{d\epsilon_1}{d\epsilon_2} = -\frac{[X_1(t+dt) - X_1(t)]/X_1(t)}{[X_2(t+dt) - X_2(t)]/X_2(t)}. \quad (7)$$

The expression for the Poisson's ratio of the auxetic structure at various deformation lengths, along with its detailed derivation, is provided in Appendix A.

The initial Poisson's ratio of the ideal single-cell rotating triangular auxetic structure, as derived from the above theoretical analysis, depends solely on the vertex angle  $\delta$  and the initial angle  $\theta$ . As the structure undergoes continuous deformation, its Poisson's ratio also changes. In the fully extended state, the Poisson's ratio approaches negative infinity, provided there is no deformation in the rigid parts. An increase in the vertex angle  $\delta$  and the initial angle  $\theta$  enhances the negative Poisson's ratio performance of the structure in its initial state, which correlates with its closer proximity to the fully extended state.

To validate the theoretical analysis, rotating triangular auxetic

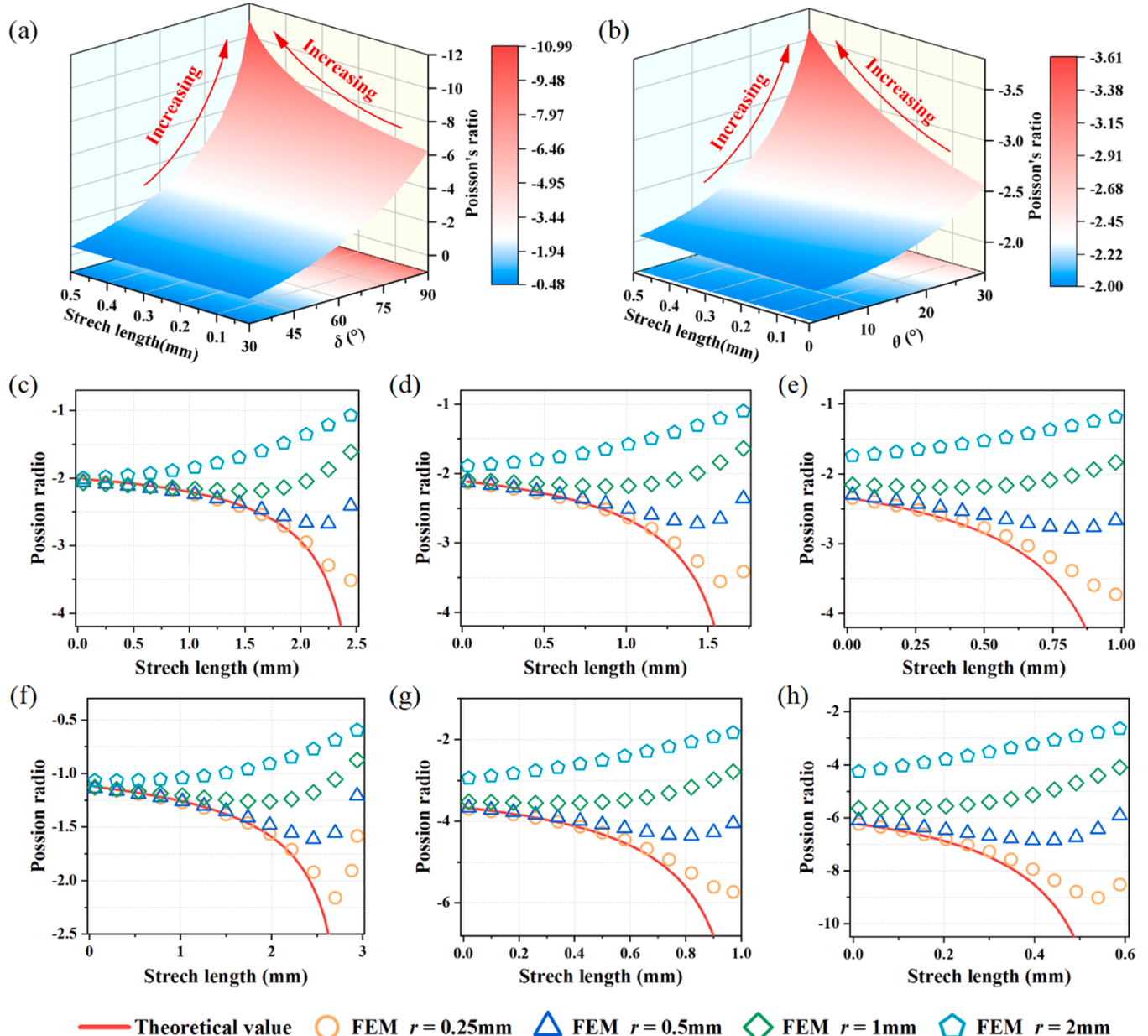


**Fig. 2.** The theoretical value of Poisson's ratio in auxetic structures during tensile processes: (a)  $\theta = 15^\circ$ ; (b)  $\delta = 60^\circ$ . The theoretical and FEM simulation values of Poisson's ratio for different hinge radii: (c)  $\theta = 5^\circ$ ,  $\delta = 60^\circ$ ; (d)  $\theta = 15^\circ$ ,  $\delta = 60^\circ$ ; (e)  $\theta = 25^\circ$ ,  $\delta = 60^\circ$ ; (f)  $\theta = 15^\circ$ ,  $\delta = 45^\circ$ ; (g)  $\theta = 15^\circ$ ,  $\delta = 75^\circ$ ; (h)  $\theta = 15^\circ$ ,  $\delta = 90^\circ$ .

structures with varying vertex angles, reference hinge radii, and initial angles were modeled. The triangle's base length  $n$  was set to 10 mm. A free tetrahedral mesh was employed during the meshing process, with one end of the auxetic structure fixed, and a longitudinal displacement applied at the opposite end for steady-state analysis. The lateral deformation in auxetic structures under different geometric parameters is shown in Appendix A. The variation of Poisson's ratio with tensile length, as calculated accordingly, is shown in Fig. 2. When the reference radius  $r$  is relatively small, the theoretical and simulation values align closely. However, as  $r$  increases, the discrepancy between theoretical and simulation values increases. Additionally, as the tensile length approaches the maximum  $t_{\max}$ , the disparity between theoretical and simulation values further increases. FEM simulation results reveal that each structure exhibits a minimum Poisson's ratio, referred to as the ultimate negative Poisson's ratio. Contrary to the theoretical prediction, the negative Poisson's ratio does not approach negative infinity.

This divergence arises due to the increased stiffness of the flexible

hinge as its radius expands, reducing the stiffness difference between the rigid parts and the flexible hinges. Consequently, during stretching, the rigid parts inevitably undergo significant deformation, diminishing the negative Poisson's ratio characteristics of the auxetic structure. Overall, a larger vertex angle  $\delta$  and a smaller reference hinge radius  $r$  lead to a smaller ultimate negative Poisson's ratio, while the initial angle  $\theta$  has minimal impact on the ultimate negative Poisson's ratio but influences the initial Poisson's ratio of the auxetic structure.

From the above analysis, it is evident that by altering the side length  $m$ , initial angle  $\theta$ , and vertex angle  $\delta$  of each triangle, different structural dimensions can be achieved. The inclusion of multiple rotating triangular unit cells within the auxetic structure further enhances its flexibility, resulting in distinct mechanical properties. When the auxetic structure comprises  $i$  unit cells per row and  $j$  unit cells per column, it is referred to as an  $i \times j$  auxetic structure, as shown in Fig. 3.

In the auxetic structure, rigid triangles can be categorized into three types: fully connected triangles, partially connected triangles, and fixed

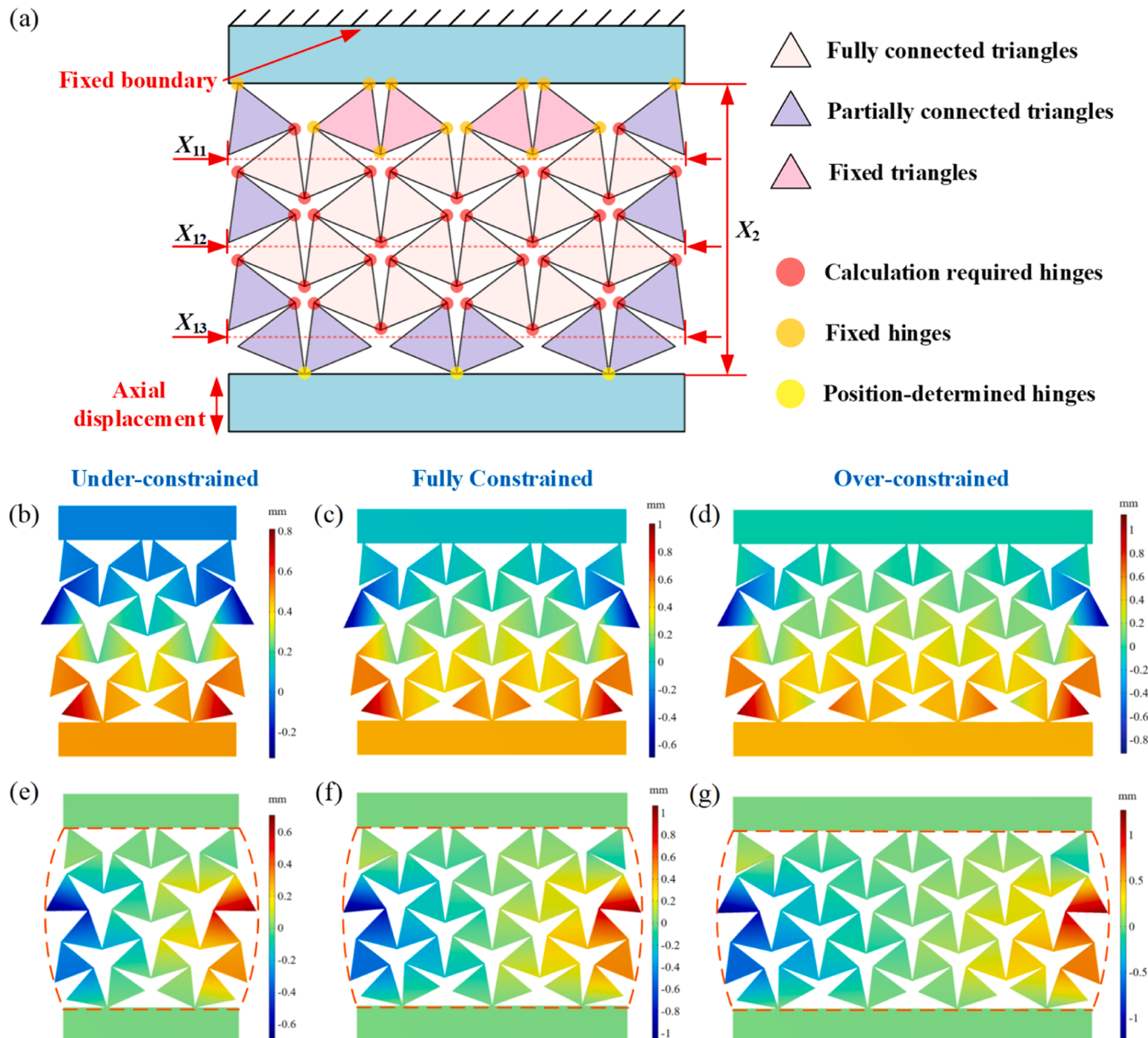


**Fig. 3.** (a) Different types of hinges and triangles in auxetic structures. FEM simulation results of longitudinal deformation in auxetic structures under tensile loading: (b)  $2 \times 3$  auxetic structure; (c)  $3 \times 3$  auxetic structure; (d)  $4 \times 3$  auxetic structure. Lateral deformation: (e)  $2 \times 3$  auxetic structure; (f)  $3 \times 3$  auxetic structure; (g)  $4 \times 3$  auxetic structure.

triangles. Similarly, flexible hinges can be categorized into three types: position-determined hinges, fixed hinges, and calculation required hinges. Since the calculation required hinges cannot be directly determined in both the X and Y directions, it is ideally assumed that each such hinge contributes two degrees of freedom during the deformation of the auxetic structure. A fully connected triangle, with all three sides attached to these hinges, provides three constraints. A partially connected triangle, with only one side attached to the calculation required hinge, contributes a single constraint, whereas a completely fixed triangle offers no constraints. Consequently, the number of constraints  $n_{\text{constraint}}$  and degrees of freedom  $n_{\text{free}}$  in the arrayed auxetic structure during stretching can be represented by the following expressions:

$$n_{\text{free}} = 12ij - 12i - 2j + 6, \quad (8)$$

$$n_{\text{constraint}} = 12ij - 10i - 4j + 6. \quad (9)$$

The detailed derivation of the  $n_{\text{constraint}}$  and  $n_{\text{free}}$  for the arrayed auxetic structure is presented in Appendix A. When  $i = j$ , the number of constraints  $n_{\text{constraint}}$  equals the number of degrees of freedom  $n_{\text{free}}$  in the structure. Under the ideal condition where the rigid plates do not deform, the positions of the hinges within the structure are fully determined, resulting in a unique solution. Therefore, this structure is referred to as fully constrained. When  $i > j$ , the number of constraints exceeds the number of degrees of freedom. In this case, if the rigid plates do not deform, the structure cannot stretch or compress, and thus it is termed over-constrained. Conversely, when  $i < j$ , the number of constraints is less than the number of degrees of freedom, leading to multiple possible solutions for the hinge positions under ideal conditions. However, during deformation, the deformation energy should always remain minimized, hence it is called under-constrained.

FEM simulation analyses of auxetic structures with various unit cell numbers were conducted. The vertex angle  $\delta$  was set to  $60^\circ$ , the included

angle  $\theta$  to  $15^\circ$ , and the stretching length  $t$  to 0.5 mm. To maintain a consistent overall length  $X_2$  of the structure, the base length  $m$  of the triangles was set to  $(10 / j)$  mm, and the reference hinge radius  $r$  to  $(0.5 / j)$  mm. The deformation contour plots in the X and Y directions were obtained, showing that certain sections of the structure experience greater lateral deformation during stretching. This suggests that the Poisson's ratio in the longitudinal direction also varies. Hence, this paper introduces the concept of an average Poisson's ratio  $\nu_{12\text{aver}}$  to better represent the overall Poisson's ratio of the structure, which is defined as follows:

$$\nu_k = -\frac{[X_{1k}(t + dt) - X_{1k}(t)]/X_{1k}(t)}{[X_2(t + dt) - X_2(t)]/X_2(t)} (k = 1, 2 \dots j), \quad (10)$$

$$\nu_{12\text{aver}} = \frac{\sum_{k=1}^j \nu_k}{j}. \quad (11)$$

The trend of the average negative Poisson's ratio with respect to tensile length for varying numbers of unit cells was calculated, as illustrated in Fig. 4. It was observed that for the same number of unit cells  $j$  in each column, the negative Poisson's ratio performance of fully constrained and under-constrained structures is significantly superior to that of over-constrained structures. This discrepancy is attributed to the unavoidable rigid parts deformation in over-constrained structures, which substantially weakens their negative Poisson's ratio performance. Consequently, to achieve optimal negative Poisson's ratio characteristics in structural design, it is advisable to ensure  $(j \geq i)$ . Notably, for fully constrained structures, as  $i$  and  $j$  increase, the average Poisson's ratio gradually rises, approaching the negative Poisson's ratio of  $-1$  [77], characteristic of triangular auxetic structures under unconstrained free rotational conditions. This indicates that as the number of unit cells continues to increase, the influence of lateral constraints at both ends on

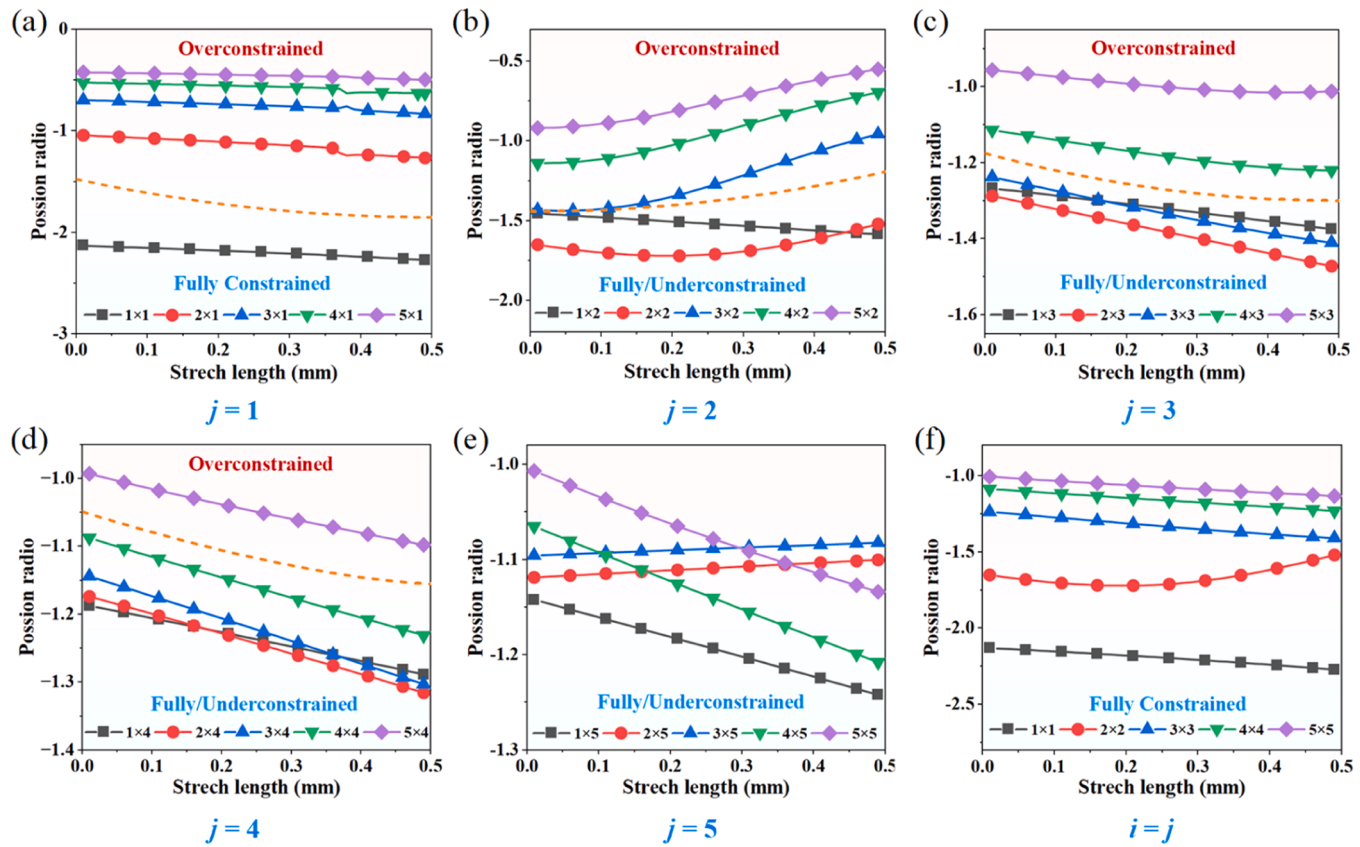


**Fig. 4.** FEM simulation results of Poisson's ratio for auxetic structures with different unit cell numbers: (a)  $j = 1$ ; (b)  $j = 2$ ; (c)  $j = 3$ ; (d)  $j = 4$ ; (e)  $j = 5$ ; (f)  $i = j$ .

the auxetic structure progressively diminishes.

### 3. Design of the auxetic-enhanced energy harvester

This section analyzes the basic principles of enhancing piezoelectric energy harvesting performance using an auxetic structure. The auxetic structure is combined with a cantilever beam piezoelectric energy harvester to design the auxetic-enhanced energy harvester (AEH) and a plate substrate energy harvester (PEH) for comparison. A finite element model is developed and optimized, and modal analysis, as well as displacement and stress distribution contour plots on the piezoelectric patch, are solved through simulations. The results demonstrate that the auxetic structure contributes to the improvement of piezoelectric energy harvesting performance.

For piezoelectric materials, the piezoelectric constitutive equation exists [78]:

$$S_1 = s_{11}^E T_1 + d_{31} E_3, \quad (12)$$

$$D_3 = d_{31} T_1 + \varepsilon_{33}^T E_3, \quad (13)$$

where  $S_1$ ,  $T_1$ ,  $E_3$ , and  $D_3$  denote the strain along 1-axis, stress along 1-axis, electric field along 3-axis, and electrical displacement along 3-axis.  $s_{11}^E$ ,  $d_{31}$ , and  $\varepsilon_{33}^T$  represent the elastic, piezoelectric, and permittivity constants. When the piezoelectric material is isotropic and satisfies the plane stress condition, its output power is given by [79]:

$$P \propto (\bar{\sigma}_{11} + \bar{\sigma}_{22})^2, \quad (14)$$

where  $\bar{\sigma}_{11}$  and  $\bar{\sigma}_{22}$  are the average longitudinal and lateral stresses in the piezoelectric material, respectively. Maintaining the same sign of average stress in both directions and increasing the average stress applied to the piezoelectric material can enhance the output power [80]. However, in conventional planar substrate piezoelectric energy harvesters, the average stresses in the two directions of the piezoelectric material have opposite signs due to the positive Poisson's ratio characteristics of both the substrate and the piezoelectric material, which is detrimental to the generation of electrical energy [81]. To address this issue, this paper proposes an AEH, composed of a clamp, brass sheet, steel beam, piezo patch, epoxy layer, and proof mass, as illustrated in

**Fig. 5.** The clamp is fabricated from PLA using 3D printing, and the steel beam is made of 65Mn steel, with one end fixed to the clamp. An auxetic structure is laser-cut into the steel beam near the clamp. The brass sheet is fully adhered over the auxetic structure using an epoxy layer, and the piezo patch, made of PZT-5H, is similarly bonded to the brass sheet with an epoxy layer. The proof mass, made of steel, is fixed at the other end of the steel beam. To demonstrate the effectiveness of the auxetic structure in enhancing energy harvesting performance, a plain beam was substituted for the auxetic beam, and a PEH was designed for comparison. The length, width, and thickness of the plain beam and auxetic beam are identical, and the dimensions of the other components are also identical.

FEM simulation was performed on AEH and PEH, with the geometric parameters and material properties specified in [Tables 1 and 2](#). During the simulation, the energy harvester is modeled as a composite system, incorporating the solid mechanics field, electrostatic field, and circuit interface, with fixed constraints applied at the base of the clamp. The electrostatic field includes only the piezoelectric patch to maintain

**Table 1**  
Geometric parameters in the AEH and the PEH.

| Part                | Parameter   | Symbol   | Value | Unit |
|---------------------|-------------|----------|-------|------|
| Beam                | Length      | $L_b$    | 200   | mm   |
|                     | Width       | $W_b$    | 25    | mm   |
|                     | Thickness   | $T_b$    | 3     | mm   |
| Piezoelectric patch | Length      | $L_p$    | 20    | mm   |
|                     | Width       | $W_p$    | 25    | mm   |
|                     | Thickness   | $T_p$    | 0.2   | mm   |
| Brass sheet         | Length      | $L_c$    | 25    | mm   |
|                     | Width       | $W_c$    | 25    | mm   |
|                     | Thickness   | $T_c$    | 0.2   | mm   |
| Proof mass          | Length      | $L_m$    | 15    | mm   |
|                     | Width       | $W_m$    | 25    | mm   |
|                     | Thickness   | $T_m$    | 6.8   | mm   |
| Auxetic structure   | Side length | $m$      | 11.85 | mm   |
|                     | $n$         | 11.85    | mm    |      |
|                     | Angle       | $\delta$ | 60    | °    |
|                     | $\theta$    | 15       | °     |      |
|                     | Radius      | $r$      | 1     | mm   |
|                     | Width       | $X_1$    | 25    | mm   |
|                     | Length      | $X_2$    | 18.96 | mm   |

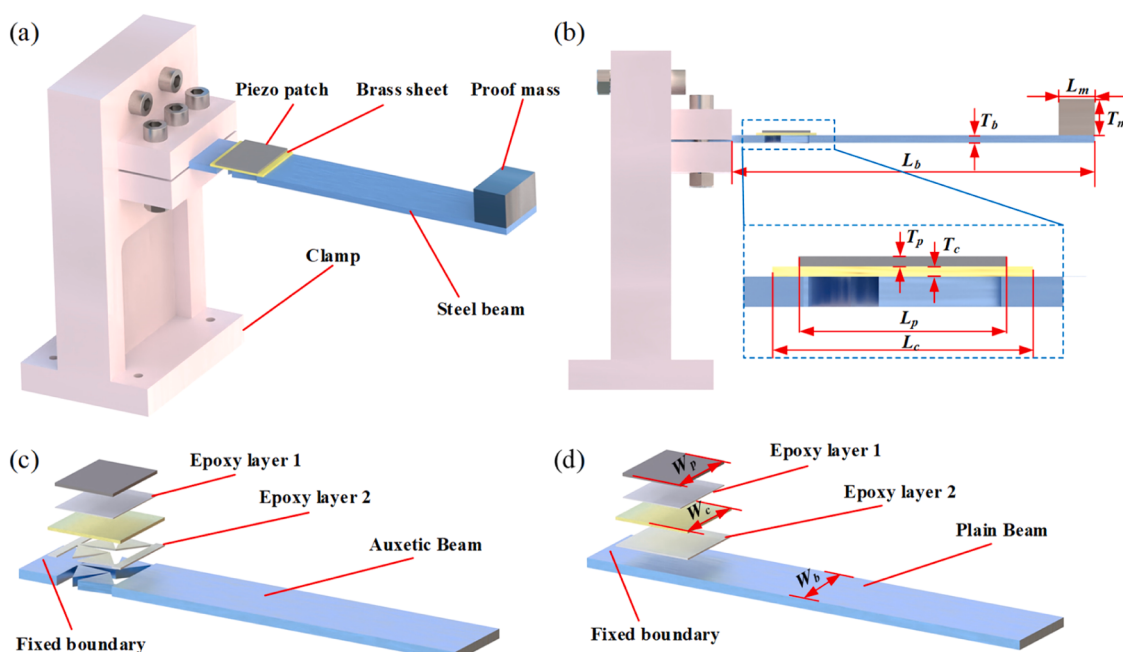


**Fig. 5.** (a) Isometric and (b) side views of the AEH. Exploded views of the (c) AEH and (d) PEH.

**Table 2**

Material properties in the AEH and the PEH.

| Material        | Parameter         | Symbol     | Value     | Unit              |
|-----------------|-------------------|------------|-----------|-------------------|
| 65Mn Steel      | Density           | $\rho_s$   | 7850      | kg/m <sup>3</sup> |
|                 | Poisson's ratio   | $\nu_s$    | 0.3       |                   |
|                 | Young's modulus   | $E_s$      | 206       | GPa               |
| Brass           | Density           | $\rho_b$   | 8470      | kg/m <sup>3</sup> |
|                 | Poisson's ratio   | $\nu_b$    | 0.35      |                   |
|                 | Young's modulus   | $E_b$      | 105       | GPa               |
| Exopy           | Density           | $\rho_e$   | 1250      | kg/m <sup>3</sup> |
|                 | Poisson's ratio   | $\nu_e$    | 0.35      |                   |
|                 | Young's modulus   | $E_e$      | 1         | GPa               |
| PLA             | Density           | $\rho_A$   | 1250      | kg/m <sup>3</sup> |
|                 | Poisson's ratio   | $\nu_A$    | 0.35      |                   |
|                 | Young's modulus   | $E_A$      | 1         | GPa               |
| PZT-5H          | Density           | $P_p$      | 7500      | kg/m <sup>3</sup> |
|                 | Compliance Matrix | $S_{11}^E$ | 1.65e-11  | 1/Pa              |
|                 |                   | $S_{12}^E$ | -4.78e-12 | 1/Pa              |
|                 |                   | $S_{13}^E$ | -8.45e-12 | 1/Pa              |
|                 |                   | $S_{22}^E$ | 1.65e-11  | 1/Pa              |
|                 |                   | $S_{23}^E$ | -8.45e-12 | 1/Pa              |
|                 |                   | $S_{33}^E$ | 2.07e-11  | 1/Pa              |
|                 |                   | $S_{44}^E$ | 4.35e-11  | 1/Pa              |
|                 |                   | $S_{55}^E$ | 4.35e-11  | 1/Pa              |
|                 |                   | $S_{66}^E$ | 4.26e-11  | 1/Pa              |
| Coupling matrix | $d_{31}$          | -2.74e-10  | C/N       |                   |
|                 | $d_{32}$          | -2.74e-10  | C/N       |                   |
|                 | $d_{33}$          | 5.93e-10   | C/N       |                   |
|                 | $d_{24}$          | 7.41e-10   | C/N       |                   |
|                 | $d_{15}$          | 7.41e-10   | C/N       |                   |

charge conservation, with both sides of the piezoelectric patch connected to resistors. A free tetrahedral mesh is employed for meshing, and mesh independence is confirmed. Material properties and damping are iteratively adjusted to align the simulation results with actual conditions. For the calculation, a frequency domain analysis is conducted, and an acceleration of 0.1g is applied along the Z-axis. The mesh division and mode shapes of AEH and PEH are shown in Fig. 6. The stress distribution on the piezo patch, along with the lateral and longitudinal deformation under resonant conditions, are shown in Fig. 7.

The results indicate that the auxetic structure can reduce the first natural frequency of the energy harvester, which is advantageous for harvesting low-frequency energy from the environment. The auxetic structure was found to cause localized stress concentrations. Compared to PEH, the stress on the piezoelectric patch in AEH is significantly higher. When the piezoelectric patch is directly bonded to the auxetic beam, the stress distribution is highly uneven, resulting in significant stress concentration and increasing the likelihood of rupture. However, when a brass sheet is introduced between the piezoelectric patch and the auxetic beam, the average stress on the patch remains nearly unchanged, while the stress distribution becomes significantly more uniform, thereby enhancing its ability to withstand large amplitude environmental vibrations.

Furthermore, the deformation contours of the piezo patch reveal that in PEH, the transverse strain is opposite to the longitudinal strain, demonstrating an overall positive Poisson's ratio characteristic. In contrast, AEH exhibits a significant region with a negative Poisson's ratio, where the transverse and longitudinal strains in the piezo patch are of the same sign, which is also beneficial for enhancing the output power of the piezo patch. At the same time, this implies that when the piezoelectric cantilever beam undergoes bending vibrations under environmental stimulation, the tensile structure experiences longitudinal stretching and compression. However, it is important to note that a region with a positive Poisson's ratio still exists in the piezoelectric patch of the AEH. This occurs primarily because the brass sheet and the piezoelectric patch itself retain positive Poisson's ratio characteristics, which diminishes the impact of the auxetic beam. Additionally, the bending deformation of the cantilever beam, rather than purely longitudinal stretching, contributes to the formation of this positive Poisson's ratio region. Nonetheless, FEM simulations demonstrate that structures with a larger longitudinal tensile negative Poisson's ratio generally exhibit improved negative Poisson's ratio performance in the piezoelectric patch.

#### 4. Comparison between theoretical and experimental results

This section presents the fabrication of prototypes for both the AEH

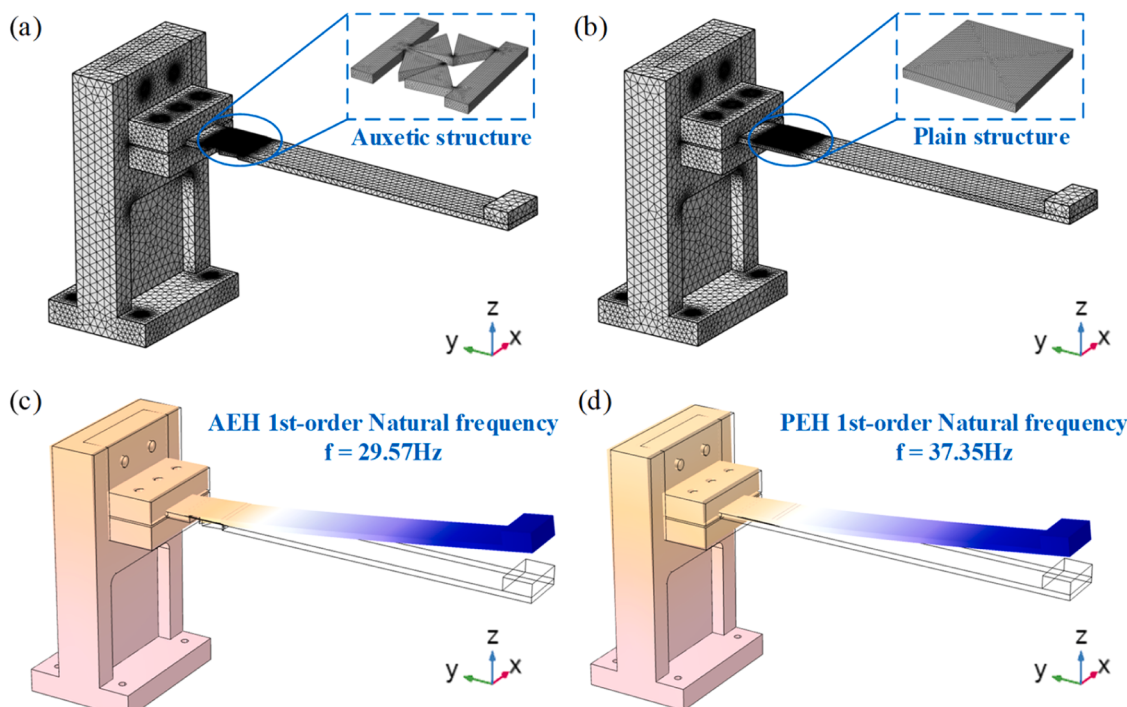


**Fig. 6.** Mesh Division in FEM Simulation of the (a) AEH and (b) PEH. First-order natural frequencies of (c) AEH and (d) PEH.

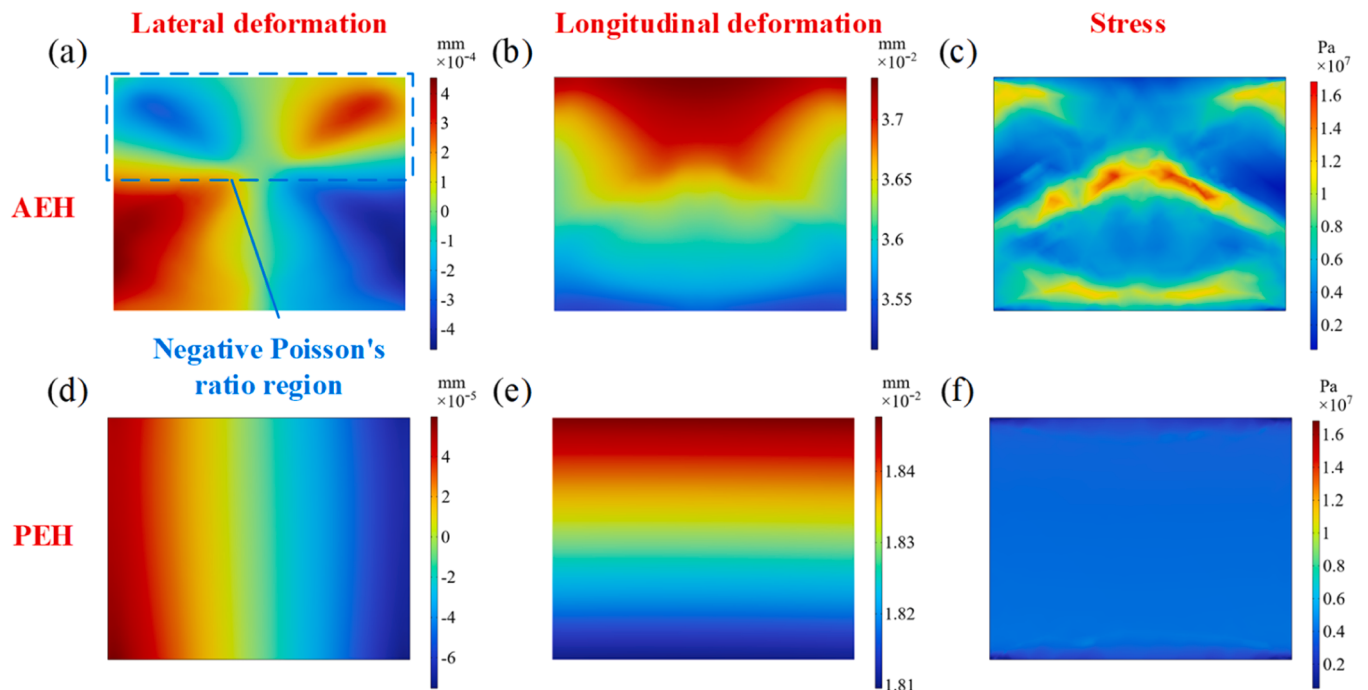


**Fig. 7.** FEM simulation results at First-order resonance of the structure: (a) Lateral deformation; (b) longitudinal deformation; (c) stress in the piezoelectric patch of the AEH. (d) Lateral deformation; (e) longitudinal deformation; (f) stress in the piezoelectric patch of the PEH.

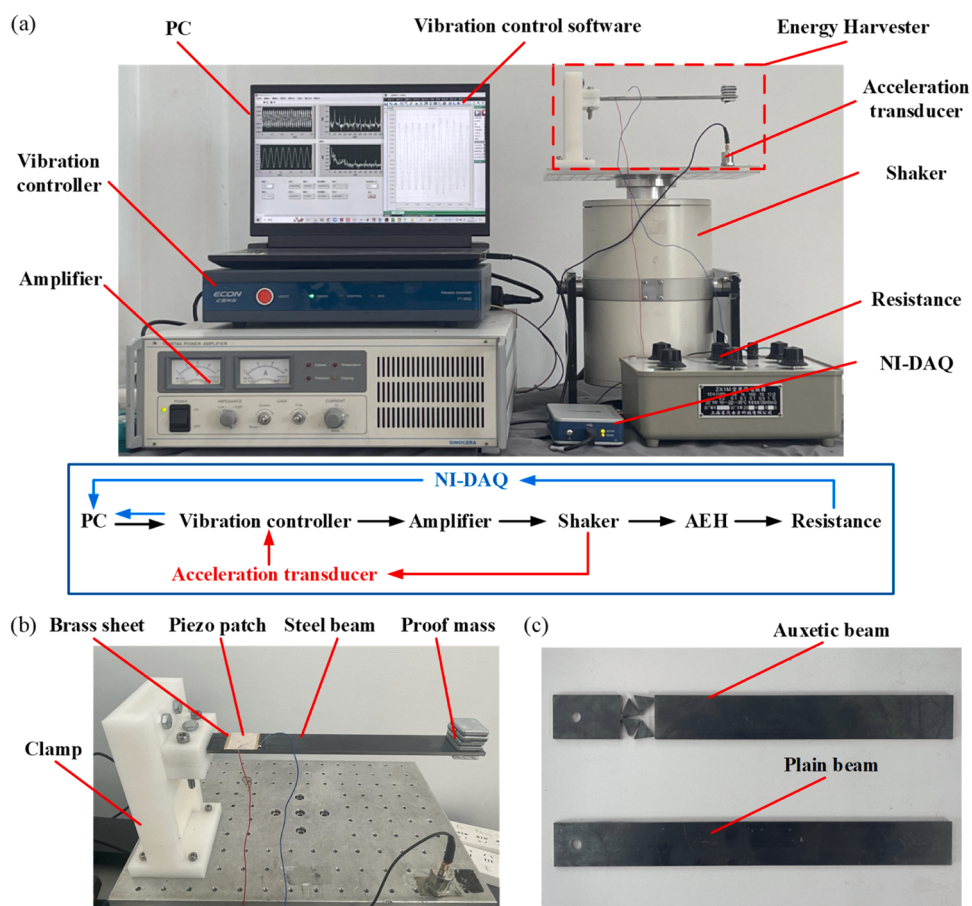


**Fig. 8.** (a) Experimental setup for vibration-based energy harvesting. (b) Energy harvester. (c) The auxetic beam and the plain beam.

and PEH, along with the construction of an experimental platform. The experimental results confirm the accuracy of the previously conducted finite element simulations. Furthermore, the results indicate that the energy harvesting performance of the AEH is consistently superior to

that of the PEH, regardless of variations in unit cell numbers and geometric parameters.

To validate the effectiveness of the proposed AEH, both AEH and PEH are fabricated, and an experimental platform is established, as

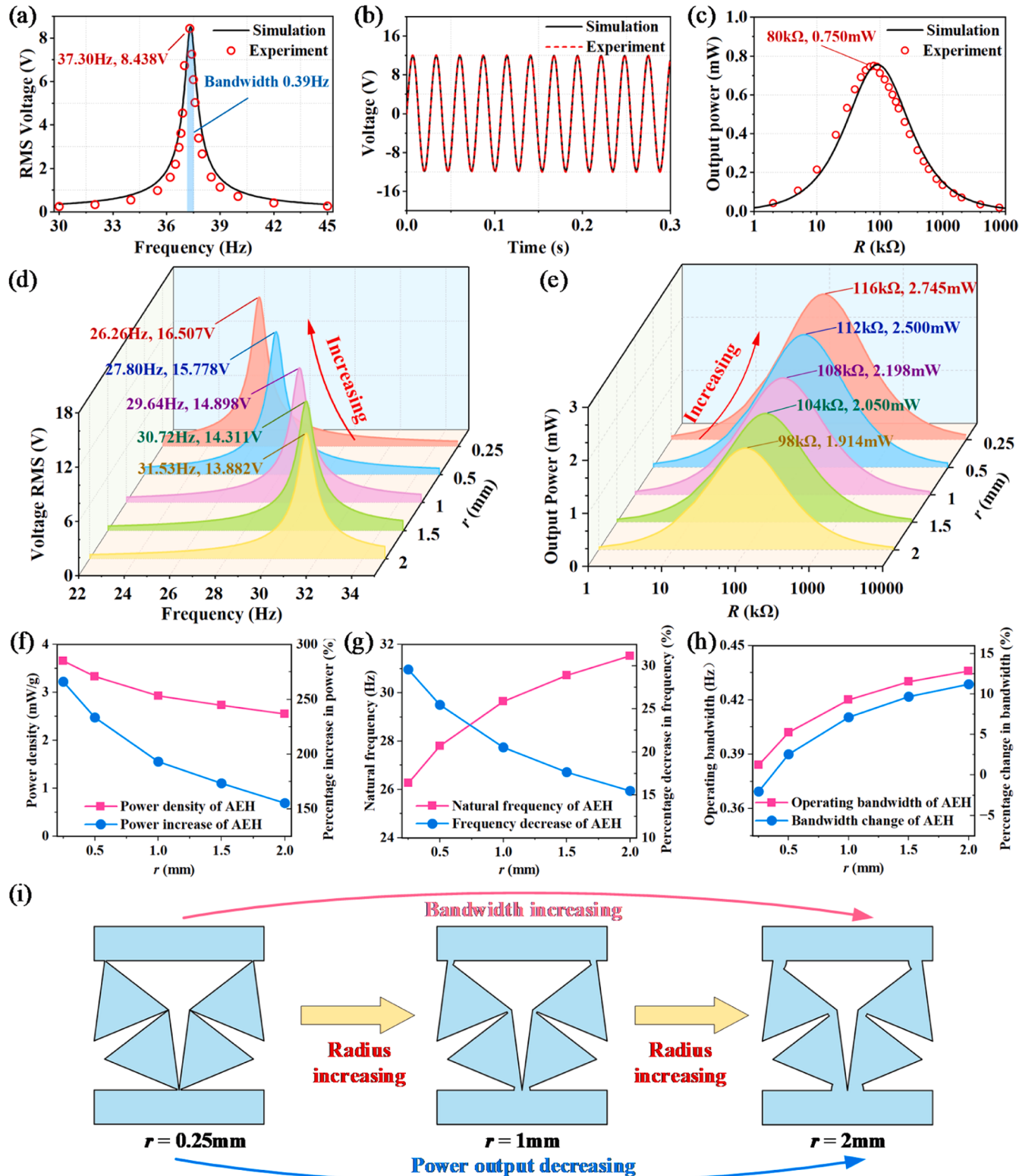


**Fig. 9.** Results of FEM simulation and experiment for PEH: (a) Variation of RMS voltage with excitation frequency; (b) Variation of output voltage with time at resonance; (c) Variation of output power with resistance during at resonance. (d) Variation of output RMS voltage with excitation frequency for AEH under different hinge radii. (e) Variation of output power with resistance for AEH under different hinge radii. The variation of AEH compared to PEH: (f) Power density; (g) Natural frequency; (h) Operating bandwidth. (i) Auxetic structures with different hinge radii.

shown in Fig. 8. The platform comprises a PC, shaker, vibration controller, amplifier, piezoelectric energy harvester, resistance, acceleration transducer, and NI-DAQ. During operation, the vibration control software on the computer modifies the acceleration, frequency, waveform, and variation of these parameters over time for the vibration excitation. The vibration controller sends control signals to the amplifier, which drives the shaker to vibrate. The acceleration transducer, fixed to the shaker using a magnet, collects real-time acceleration data during vibration, converting it into electrical signals that are sent back to the vibration controller for closed-loop control. The shaker and energy harvester are bolted together to achieve synchronous vibration. During this process, the piezo patch of the energy harvester is connected to the resistance, generating electrical energy. NI-DAQ continuously monitors the voltage across the resistor in real-time, while the PC is used for data monitoring and storage. In this study, the frequency range in which the output power of the harvester exceeds  $(\sqrt{2}/2)$  times the peak power is considered the harvester's bandwidth, and the output voltage of the harvester is represented by the root mean square (RMS) value of the voltage.

The effect of the reference hinge radius  $r$  on the energy harvesting performance of AEH is analyzed. Apart from the reference hinge radius, the dimensions of AEH and PEH are consistent with those listed in Table 1. For both PEH and the four types of AEH, the excitation acceleration was set at 0.1 g. Fig. 9 presents the results of FEM simulations and experiments. The simulation values and experimental results align well in terms of the time-domain characteristics of the harvester's output voltage, frequency-domain characteristics, and the variation of output power with load resistance, demonstrating the reliability of the FEM simulations. The slight discrepancies between the simulation and experimental values may be attributed to inaccuracies in material properties, as well as errors in manufacturing and assembly.

Under a 100 k $\Omega$  load resistance, the peak RMS voltage of the PEH is 8.44 V, corresponding to a frequency of 37.30 Hz, a bandwidth of 0.39 Hz, and a peak output power of 0.750 mW at a resistance of 80 k $\Omega$ . For AEH, as the reference hinge radius increases from 0.25 mm to 2 mm, the natural frequency rises from 26.26 Hz to 31.53 Hz, while the peak RMS voltage under a 100 k $\Omega$  load decreases from 16.507 V to 13.882 V, and the bandwidth expands from 0.384 Hz to 0.436 Hz. The peak output power of AEH decreases from 2.745 mW to 1.914 mW, with the corresponding load resistance increasing from 98 k $\Omega$  to 116 k $\Omega$ . As the hinge radius increases, the natural frequency of AEH gradually increases, and the peak output power continuously decreases. Compared to PEH, AEH with different hinge radii can enhance output power by 155.3 % to 266.1 % and reduce the natural frequency by 15.5 % to 29.6 %. However, a larger hinge radius contributes to expanding the bandwidth of AEH. When the reference hinge radius is 0.25 mm, AEH reduces the bandwidth by 2.0 % compared to PEH, whereas when the radius increases to 2 mm, AEH increases the bandwidth by 11.2 % compared to PEH.

The occurrence of this phenomenon is due to the fact that as the hinge radius increases, the stiffness of the auxetic beam also increases, which in turn raises the natural frequency of the AEH. An increased hinge radius negatively affects the negative Poisson's ratio performance of the auxetic structure and reduces the stress concentration effect. This results in a decrease in the average stress within the piezoelectric patch and further weakens the negative Poisson's ratio performance, ultimately diminishing the energy output of the AEH. However, the auxetic structure exhibits mechanical nonlinearities during stretching and bending, where both stiffness and Poisson's ratio vary with deformation. As a result, the bandwidth of the AEH also changes with the hinge radius.

In piezoelectric energy harvesters, the dimensions of the piezoelectric patches often vary. By adjusting the vertex angle of the triangles in the auxetic structure, piezoelectric patches with different length-to-width ratios can be accommodated. The triangle vertex angle  $\delta$  can

vary from 45° to 105°, while keeping the isosceles triangle base length  $n$  fixed at 11.85 mm, the reference radius  $r$  at 1 mm, and the angle  $\theta$  at 15°. The structural dimensions of PEH and AEH under different vertex angles are shown in Appendix A. Since the length of the auxetic structure changes minimally, the lengths of the piezoelectric patch and brass sheet also remain unchanged at 20 mm and 25 mm, respectively. However, the widths of the steel beam, piezoelectric patch, and brass sheet change with the width of the auxetic structure. The dimensions and position of the proof mass remain constant, with the mass consistently maintained at 20 g.

As shown in Fig. 10, for AEH, as the vertex angle  $\delta$  increases from 45° to 105°, the natural frequency varies from 27.45 Hz to 30.64 Hz, while the peak power decreases from 2.93 mW to 1.44 mW, and the optimal resistance increases from 87 k $\Omega$  to 170 k $\Omega$ . Similarly, for PEH, as the vertex angle  $\delta$  increases from 45° to 105°, the natural frequency ranges from 35.83 Hz to 37.30 Hz, with the peak power decreasing from 0.88 mW to 0.54 mW. It is noteworthy that as the vertex angle  $\delta$  increases, the weight of the piezo patch gradually decreases. Consequently, although the peak power decreases for both PEH and AEH, the power density consistently increases. Compared to PEH, AEH enhances power density by 166.0 % to 233.3 % across different vertex angles. However, as the vertex angle increases, AEH achieves a broader bandwidth than PEH, but its ability to reduce the natural frequency diminishes. When the vertex angle is 45°, AEH reduces the natural frequency by 25.81 % and increases the bandwidth by 0.52 % compared to PEH. At a vertex angle of 105°, AEH reduces the natural frequency by 15.35 % and increases the bandwidth by 13.23 % compared to PEH.

Overall, as the vertex angle increases, the negative Poisson's ratio characteristic of the auxetic structure is enhanced, leading to an increase in the energy density of the piezo patch. However, as the area of the auxetic structure decreases while the reference hinge radius remains unchanged, the stiffness ratio between the flexible hinge and the rest of the structure increases, which subsequently weakens the effect of reducing the natural frequency.

Altering the unit cell numbers in the auxetic structure can accommodate piezoelectric patches of various sizes. Set the triangle's vertex angle  $\delta$  to 60°, the base length  $n$  to 11.85 mm, the reference radius  $r$  to 1 mm, and the angle  $\theta$  to 15°, with the unit cell numbers varying from 1 × 1 to 1 × 5. The structural dimensions of PEH and AEH under different unit cell numbers are listed in Appendix A. The length of the steel beam  $L_b$  remains constant. As the width of the auxetic structure is unchanged, the widths of the piezoelectric patch, brass sheet, and steel beam remain constant as well. However, the lengths of the piezoelectric patch and brass sheet vary with the length of the auxetic structure. The size of the proof mass remains constant, with the mass maintained at 20 g.

The energy harvesting characteristics of AEH and PEH with different unit cell numbers are shown in Fig. 11. As the unit cell numbers in the AEH increases from 1 × 1 to 1 × 5, the natural frequency decreases from 29.63 Hz to 21.78 Hz. Conversely, for the corresponding PEH, the natural frequency increases from 37.30 Hz to 37.98 Hz as the number of unit cells increases. Compared to PEH, the 1 × 5 AEH reduces the natural frequency by 42.65 %. As the cell numbers increase, the peak power of AEH rises from 2.198 mW to 3.117 mW, with the corresponding load resistance decreasing from 108 k $\Omega$  to 43 k $\Omega$ . For PEH, the peak power increases from 0.750 mW to 1.588 mW, with the corresponding load resistance decreasing from 80 k $\Omega$  to 25 k $\Omega$ . However, as the weight of the piezoelectric patch increases with the cell numbers, the energy density of AEH decreases from 2.93 mW/g to 1.054 mW/g, while that of PEH decreases from 1.00 mW/g to 0.54 mW/g. The energy density enhancement effect of the AEH decreases from 193.2 % to 96.3 %. In terms of bandwidth, as the cell numbers increase, the bandwidth of AEH decreases rapidly, while that of PEH remains almost unchanged. For the 1 × 1 structure, the bandwidth of AEH is 0.42 Hz, compared to 0.392 Hz for PEH, representing a 7.1 % increase in bandwidth for AEH. However, for the 1 × 5 structure, the bandwidth of AEH is 0.300 Hz, compared to 0.410 Hz for PEH, representing a 26.8 % decrease in bandwidth for AEH.

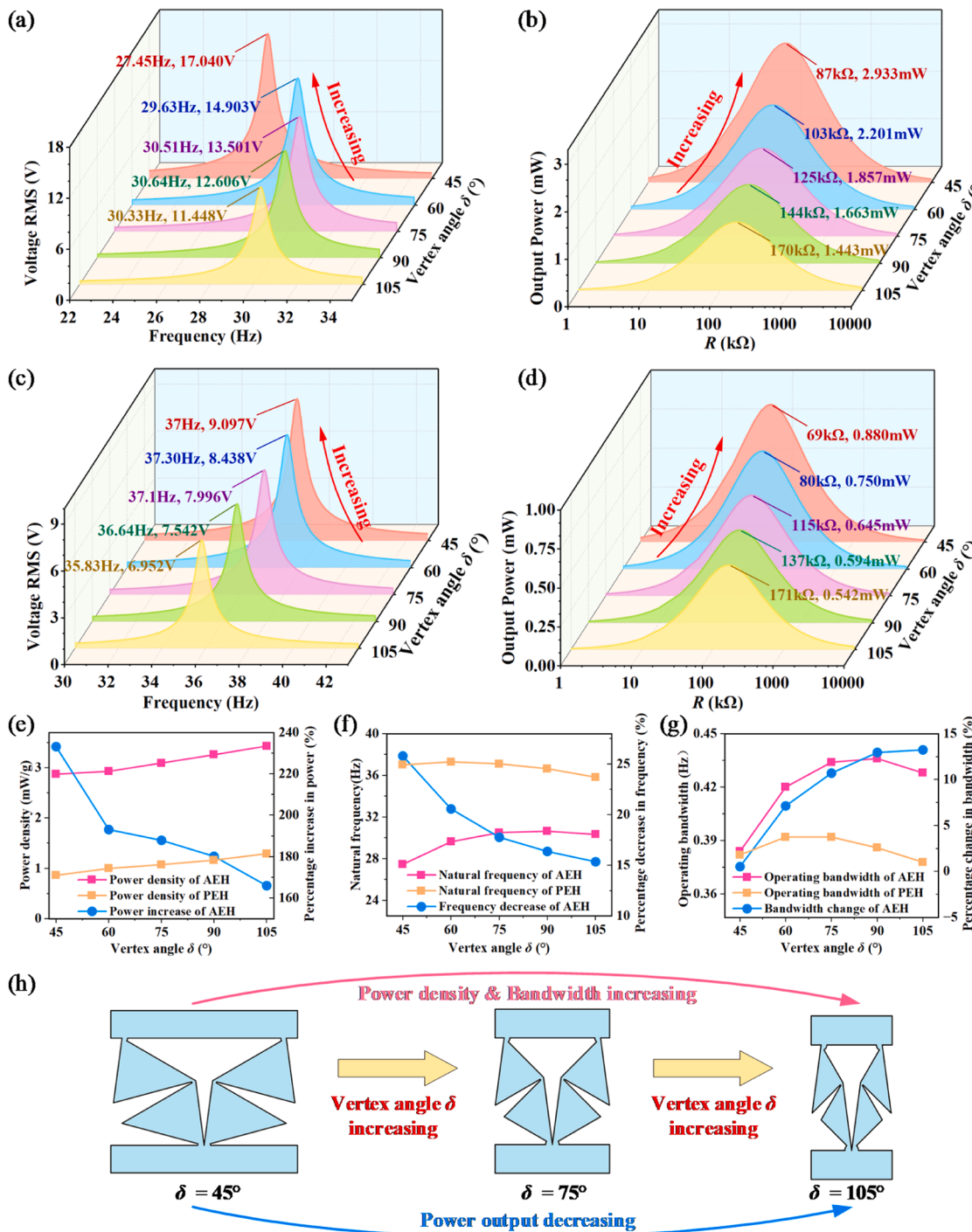


**Fig. 10.** (a) Variation of RMS output voltage with frequency and (b) Variation of output power with resistance for AEH under different vertex angles. (c) Variation of RMS output voltage with frequency and (d) Variation of output power with resistance for PEH under different vertex angles. The variation of AEH compared to PEH: (e) Power density; (f) Natural frequency; (g) Operating bandwidth. (h) Auxetic Structures with different vertex angles.

This phenomenon occurs because, in the PEH, as the unit cell numbers increase, the lengths of both the brass sheet and piezoelectric patch also increase, thereby enhancing the stiffness of the piezoelectric beam. In contrast, in the AEH, an increase in the proportion of the steel beam auxetic structure significantly reduces the stiffness of the piezoelectric beam, resulting in a rapid decrease in the natural frequency. Additionally, as the unit cell numbers increase, the negative Poisson's ratio characteristics of the auxetic structure diminish, and the stress distribution in the piezoelectric patch becomes more uneven. The stress further decreases from the fixed end, which hampers the increase in the

average stress in the piezoelectric patch, leading to a rapid reduction in the energy density of the AEH. A similar phenomenon occurs in the PEH, where the stress distribution becomes more uneven with an increase in the length of the piezoelectric patch; however, this effect is less pronounced than in the AEH. Overall, as the unit cell numbers increase, both the energy density and bandwidth of the AEH decrease, while its ability to reduce the natural frequency improves.

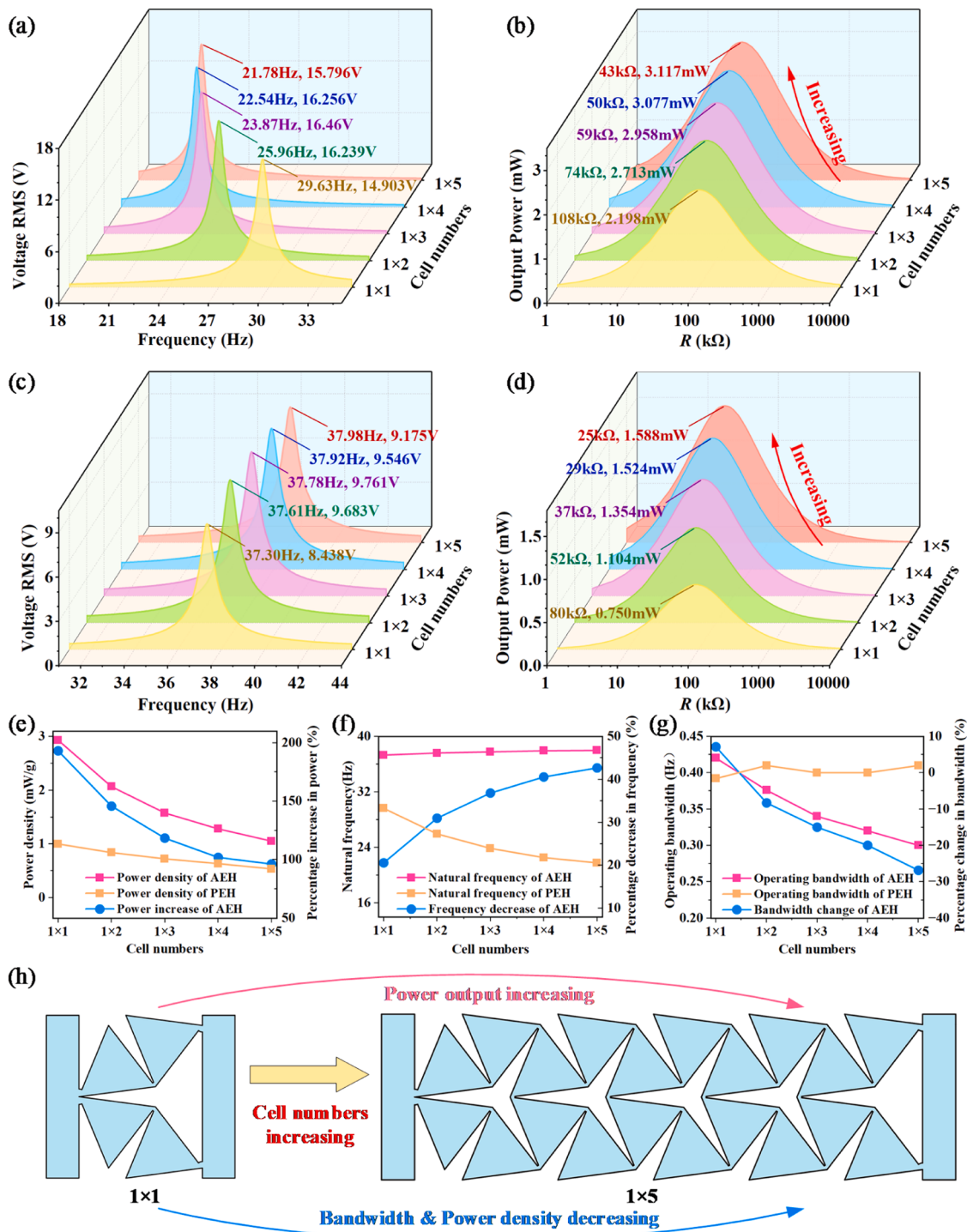


**Fig. 11.** (a) Variation of RMS output voltage with frequency and (b) Variation of output power with resistance for AEH under different cell numbers. (c) Variation of RMS output voltage with frequency and (d) Variation of output power with resistance for PEH under different cell numbers. The variation of AEH compared to PEH: (e) Power density; (f) Natural frequency; (g) Operating bandwidth. (h) Auxetic Structures with different cell numbers.

## 5. Conclusions

This study introduces a novel method that employs a rotating triangular auxetic structure to enhance the performance of piezoelectric energy harvesters. The unique mechanical properties of the auxetic structure are leveraged to improve the energy density of the piezoelectric patch and extend its bandwidth, making it more effective for harvesting low-frequency environmental energy. The more specific finding associated with this work is as follows:

A numerical solution method for the mechanical properties of the auxetic structure was developed. In the single-unit-cell auxetic structure, larger triangle vertex angles and smaller hinge radii result in improved negative Poisson's ratio characteristics, including smaller initial and ultimate negative Poisson's ratios. In the arrayed auxetic structure, the number of unit cells per row and column affects the constraint relationships, with fully constrained and under-constrained structures generally exhibiting superior negative Poisson's ratio performance compared to over-constrained structures.

An AEH was designed based on the auxetic structure, and FEM simulations were performed. The results show that, compared to the PEH, the auxetic structure in the AEH significantly increases the average stress on the piezoelectric patch and creates large areas with negative Poisson's ratios. Prototypes of the AEH and PEH were fabricated, and experimental validation was conducted. The experimental results confirmed the accuracy of the FEM simulations and revealed that, for AEHs with varying geometric parameters and unit cell numbers, output power increased by 96.3 % to 266.1 % compared to the PEH, while the natural frequency decreased by 15.35 % to 42.65 %, making the AEH more suitable for harvesting low-frequency vibration energy.

Overall, compared to the PEH, the AEH increases output power across various geometric parameters and unit cell numbers, and adapts well to piezoelectric patches with varying aspect ratios, demonstrating broad applicability. The enhanced negative Poisson's ratio characteristics of the auxetic structure enable the piezoelectric patch to exhibit a more pronounced negative Poisson's ratio, thereby contributing to increased energy density. Furthermore, appropriate selection of unit cell numbers and geometric parameters can potentially increase the energy harvester's bandwidth.

#### CRediT authorship contribution statement

**Xiaofan Zhang:** Writing – original draft, Validation, Resources, Formal analysis, Conceptualization. **Xiaobiao Shan:** Writing – review & editing, Supervision, Funding acquisition. **Guangdong Sui:** Formal analysis, Data curation, Conceptualization. **Chengwei Hou:** Data curation. **Xuteng Du:** Data curation. **Zhaowei Min:** Writing – review & editing. **Tao Xie:** Supervision.

#### Declaration of competing interest

The authors declare that they have no known competing financial interests or personal relationships that could have appeared to influence the work reported in this paper.

#### Acknowledgments

This work is supported by the National Natural Science Foundation of China (No. 52375088).

#### Supplementary materials

Supplementary material associated with this article can be found, in the online version, at doi:10.1016/j.ijmecsci.2025.110081.

#### Data availability

Data will be made available on request.

#### References

- [1] Huo S, Wang P, Long H, Ren Z, Yi Q, Dai J, et al. Dual-mode electromagnetic energy harvester by Halbach arrays. *Energy Convers Manag* 2023;286:117038.
- [2] Yu L, Tang L, Yang T. Piezoelectric passive self-tuning energy harvester based on a beam-slider structure. *J Sound Vib* 2020;489:115689.
- [3] Xu H, Zhou S. Theoretical analysis and potential engineering application of an energy harvester. *Int J Mech Sci* 2024;275:109284.
- [4] Zhang L, Zheng H, Liu B, Liang Q, Li K, Liu J, et al. A piezoelectric energy harvester for multi-type environments. *Energy* 2024;305:132218.
- [5] dos Santos LM, Santos FL, Scinocca F, Villibor GP. Piezoelectric energy harvesting in agricultural machinery: impact of PZT configurations and rectification techniques on power generation. *Energy Rep* 2025;13:455–64.
- [6] Sun L, He L, Li Z, Zhong F, Yu B, Lin J. An inclined pedal type piezoelectric energy harvester for pedestrian flow and vehicle safety monitoring. *Sustain Energy Technol Assess* 2024;63:103646.
- [7] Zhang Z, Xiang H, Tang L, Yang W. A comprehensive analysis of piezoelectric energy harvesting from bridge vibrations. *J Phys D Appl Phys* 2022;56:014001.
- [8] Han L, He L, Lv X, Sun L, Zhang L, Fan W. Piezoelectric-electromagnetic wearable harvester for energy harvesting and motion monitoring. *Sustain Energy Technol Assess* 2024;71:104030.
- [9] Zhou Z, Cao D, Huang H, Qin W, Du W, Zhu P. Biomimetic swallowtail V-shaped attachments for enhanced low-speed wind energy harvesting by a galloping piezoelectric energy harvester. *Energy* 2024;304:132063.
- [10] Li Z, Roscov J, Khanbareh H, Haswell G, Bowen C. Energy harvesting from water flow by using piezoelectric materials. *Adv Energy Sustain Res* 2024;5:2300235.
- [11] Yu H, Fan L, Shan X, Zhang X, Zhang X, Hou C, et al. A novel multimodal piezoelectric energy harvester with rotating-DOF for low-frequency vibration. *Energy Convers Manag* 2023;287:117106.
- [12] Kurt E, Issimova A, Medetov B. A wide-band electromagnetic energy harvester. *Energy* 2023;277:127693.
- [13] Jin Z, Wang L, Zheng K, Gao Q, Feng W, Hu S, et al. Microelectronic printed chitosan/chondroitin sulfate/ZnO flexible and environmentally friendly triboelectric nanogenerator. *J Colloid Interface Sci* 2024;669:275–82.
- [14] Zou D, Liu G, Rao Z, Cao J, Liao WH. Design of a high-performance piecewise bistable piezoelectric energy harvester. *Energy* 2022;241:122514.
- [15] Wu Z, Xu Q. Design of a structure-based bistable piezoelectric energy harvester for scavenging vibration energy in gravity direction. *Mech Syst Signal Process* 2022;162:108043.
- [16] Chen HH, You SK, Su WJ. The design, fabrication and analysis of a cantilever-based tensile-mode nonlinear piezoelectric energy harvester. *Mech Syst Signal Process* 2024;212:111317.
- [17] Du X, Han Y, Guo D, Wang W, Liu X, Wang S, et al. Hybrid piezo-triboelectric wind energy harvesting mechanism with flag-dragging the cantilever beam vibration. *Nano Energy* 2024;131:110274.
- [18] Guo L, Wang H. Multi-physics modeling of piezoelectric energy harvesters from vibrations for improved cantilever designs. *Energy* 2023;263:125870.
- [19] Zhang X, Huang X, Wang B. A quad-stable nonlinear piezoelectric energy harvester with piecewise stiffness for broadband energy harvesting. *Nonlinear Dyn* 2024;112:19633–52.
- [20] Yu H, Hou C, Shan X, Zhang X, Song H, Zhang X, et al. A novel seesaw-like piezoelectric energy harvester for low frequency vibration. *Energy* 2022;261:125241.
- [21] Tian H, Yurchenko D, Li Z, Guo J, Kang X, Wang J. Dumbbell-shaped piezoelectric energy harvesting from coupled vibrations. *Int J Mech Sci* 2024;281:109681.
- [22] Ma X, Chen G, Li Z, Litak G, Zhou S. Nonlinear dynamic characteristics of the multistable wake-galloping energy harvester. *Nonlinear Dyn* 2024;112:10937–58.
- [23] Zhao L, Hu G, Zhou S, Peng Y, Xie S, Li Z. Magnetic coupling and amplitude truncation based bistable energy harvester. *Int J Mech Sci* 2024;273:109228.
- [24] Du F, Wang N, Ma T, Shi R, Yin L, Li C. Design and experimental study of magnetically excited variable cross section bending beam piezoelectric energy harvester. *Appl Energy* 2024;370:123636.
- [25] Li Z, Wang S, Zhou S. Multi-solution phenomena and nonlinear characteristics of tristable galloping energy harvesters with magnetic coupling nonlinearity. *Commun Nonlinear Sci Numer Simul* 2023;119:107076.
- [26] Xie Z, Liu L, Huang W, Shu R, Ge S, Xin Y, et al. A multimodal E-shaped piezoelectric energy harvester with a built-in bistability and internal resonance. *Energy Convers Manag* 2023;278:116717.
- [27] Wang T, Zhang Q, Han J, Tian R, Yan Y, Cao X, et al. Low-frequency energy scavenging by a stacked tri-stable piezoelectric energy harvester. *Int J Mech Sci* 2024;280:109546.
- [28] Qian F, Hajji MR, Zuo L. Bio-inspired bi-stable piezoelectric harvester for broadband vibration energy harvesting. *Energy Convers Manag* 2020;222:113174.
- [29] Ma X, Li H, Zhou S, Yang Z, Litak G. Characterizing nonlinear characteristics of asymmetric tristable energy harvesters. *Mech Syst Signal Process* 2022;168:108612.
- [30] Sun S, Leng Y, Su X, Zhang Y, Chen X, Xu J. Performance of a novel dual-magnet tri-stable piezoelectric energy harvester subjected to random excitation. *Energy Convers Manag* 2021;239:114246.
- [31] Mei X, Zhou S, Yang Z, Kaizuka T, Nakano K. Enhancing energy harvesting in low-frequency rotational motion by a quad-stable energy harvester with time-varying potential wells. *Mech Syst Signal Process* 2021;148:107167.
- [32] Hu G, Tang L, Das R, Marzocca P. A two-degree-of-freedom piezoelectric energy harvester with stoppers for achieving enhanced performance. *Int J Mech Sci* 2018;149:500–7.
- [33] Lin S, Yang Z, Zhang L, Yang J, Wu S, Zhang Z, et al. Design, fabrication, and characterization of a deformation-restricted piezoelectric vibration energy harvester triggered by a stopper. *Energy* 2024;312:133550.
- [34] Zhang L, Kan J, Lin S, Liao W, Yang J, Liu P, et al. Design and performance evaluation of a pendulous piezoelectric rotational energy harvester through magnetic plucking of a fan-shaped hanging composite plate. *Renew Energy* 2024;222:119796.
- [35] Sun W, Hu S, Li H, Chen R, Zhao D. Enhancement of piezoelectric energy harvesting by the elliptical cylinder interference. *Int J Mech Sci* 2024;263:108785.
- [36] Kan J, Zhang L, Wang S, Lin S, Yang Z, Meng F, et al. Design and characterization of a self-excited unibody piezoelectric energy harvester by utilizing rotationally induced pendulation of along-groove iron balls. *Energy* 2023;285:129467.
- [37] Zhang Z, Lin S, Gu Y, Zhang L, Wang S, Zhai S, et al. Design and characteristic analysis of a novel deformation-controllable piezoelectric vibration energy harvester for low frequency. *Energy Convers Manag* 2023;286:117016.
- [38] Lin S, Yu Y, He C, Zhang Z, Yang J, Yang Z, et al. A novel pendulum-like deformation-limited piezoelectric vibration energy harvester triggered indirectly via a smoothly plucked drive plate. *Mech Syst Signal Process* 2025;224:112154.

- [39] Wang JX, Su WB, Li JC, Wang CM. A rotational piezoelectric energy harvester based on trapezoid beam: simulation and experiment. *Renew Energy* 2022;184: 619–26.
- [40] Benasciutti D, Moro I, Zelenika S, Brusa E. Vibration energy scavenging via piezoelectric bimorphs of optimized shapes. *Microsyst Technol* 2009;16:657–68.
- [41] Mohamed K, Elgamal H, Kouritem SA. An experimental validation of a new shape optimization technique for piezoelectric harvesting cantilever beams. *Alex Eng J* 2021;60:1751–66.
- [42] Piyarathna IE, Thabet AM, Ucgul M, Lemckert C, Lim YY, Tang ZS. Linear segmented arc-shaped piezoelectric branch beam energy harvester for ultra-low frequency vibrations. *Sensors* 2023;23:5257.
- [43] Wang L, Tong X, Yang H, Wei Y, Miao Y. Design and analysis of a hollow triangular piezoelectric cantilever beam harvester for vibration energy collection. *Int J Pavement Res Technol* 2019;12:259–68.
- [44] Zhang P, Lin W, Xie Z, Cao H, Huang W. I-shaped cantilever beam piezoelectric energy harvester with frequency up-conversion for ultra-low-frequency rotating environments. *Mech Syst Signal Process* 2025;225:112281.
- [45] Yu H, Zhang X, Shan X, Hu L, Zhang X, Hou C, et al. A novel bird-shape broadband piezoelectric energy harvester for low frequency vibrations. *Micromachines* 2023; 14:421 (Basel).
- [46] Shim HK, Sun S, Kim HS, Lee DG, Lee YJ, Jang JS, et al. On a nonlinear broadband piezoelectric energy harvester with a coupled beam array. *Appl Energy* 2022;328: 120129.
- [47] Wang G, Song R, Luo L, Yu P, Yang X, Zhang L. Multi-piezoelectric energy harvesters array based on wind-induced vibration: design, simulation, and experimental evaluation. *Energy* 2024;300:131509.
- [48] Dong L, Wen C, Liu Y, Xu Z, Closson AB, Han X, et al. Piezoelectric buckled beam array on a pacemaker lead for energy harvesting. *Adv Mater Technol* 2018;4: 1800335.
- [49] Na Y, Lee MS, Lee JW, Jeong YH. Horizontally assembled trapezoidal piezoelectric cantilevers driven by magnetic coupling for rotational energy harvester applications. *Energies* 2021;14:498 (Basel).
- [50] Hou C, Du X, Dang S, Shan X, Elsamaty M, Guo K, et al. A broadband and multiband magnetism-plucked rotary piezoelectric energy harvester. *Energy* 2024; 302:131846.
- [51] Wang S, Liu HT. Energy absorption performance of the auxetic arc-curved honeycomb with thickness and arc angle gradient based on additive manufacturing. *Mater Today Commun* 2023;35:105515.
- [52] Tikariha AK, Saurabh N, Gudipadu V, Patel S. Effect of auxetic structures parameters variation on PVDF-based piezoelectric energy harvesters. *J Appl Phys* 2022;132:244105.
- [53] Fatahi MH, Hamedi M, Safarabadi M. Experimental and numerical implementation of auxetic substrate for enhancing voltage of piezoelectric sandwich beam harvester. *Mech Adv Mater Struct* 2021;29:6107–17.
- [54] Grima JN, Farrugia PS, Gatt R, Attard D. On the auxetic properties of rotating rhombi and parallelograms: a preliminary investigation. *Phys Status Solidi b* 2008; 245:521–9.
- [55] Kose R, Novak N, Grednev S, Ren Z, Vesjenjak M, Jung A. Numerical prediction of the yield surface of a chiral auxetic structure. *Adv Eng Mater* 2023;26:2300914.
- [56] Jin S, Korkolis YP, Li Y. Shear resistance of an auxetic chiral mechanical metamaterial. *Int J Solids Struct* 2019;174:175:28–37.
- [57] Bohara RP, Linforth S, Nguyen T, Ghazlan A, Ngo T. Anti-blast and -impact performances of auxetic structures: a review of structures, materials, methods, and fabrications. *Eng Struct* 2023;276:115377.
- [58] Roberjot P, Herder JL. A unified design method for 2D auxetic metamaterials based on a minimal auxetic structure. *Int J Solids Struct* 2024;295:112777.
- [59] Teng XC, Jiang W, Zhang XG, Han D, Ni XH, Xu HH, et al. A stretchable sandwich panel metamaterial with auxetic rotating-square surface. *Int J Mech Sci* 2023;251: 108334.
- [60] Hou R, Dong P, Hu J, Gong Z, Sadeghzade S, Cao J, et al. An optimized lozenge-chiral auxetic metamaterial with tunable auxeticity and stiffness. *Mater Des* 2024; 237:112530.
- [61] Zhang C, Lu F, Wei T, Huang Y, He Y, Zhu Y. A novel windmill-shaped auxetic structure with energy absorption enhancement. *Int J Mech Sci* 2024;280:109635.
- [62] Li Y, Yu WR. Development of a textile structure for multi-directional auxetic deformation. *Mater Des* 2022;223:111237.
- [63] Razbin M, Bagherzadeh R, Asadnia M, Wu S. Recent advances in wearable electromechanical sensors based on auxetic textiles. *Adv Funct Mater* 2024;34: 2409242.
- [64] Ren X, Das R, Tran P, Ngo TD, Xie YM. Auxetic metamaterials and structures: a review. *Smart Mater Struct* 2018;27:023001.
- [65] Farhangdoust S, Georgeson G, Ihn JB, Chang FK. Kirigami auxetic structure for high efficiency power harvesting in self-powered and wireless structural health monitoring systems. *Smart Mater Struct* 2020;30:015037.
- [66] Chen K, Gao Q, Fang S, Zou D, Yang Z, Liao WH. An auxetic nonlinear piezoelectric energy harvester for enhancing efficiency and bandwidth. *Appl Energy* 2021;298: 117274.
- [67] Ebrahimian F, Kabirian Z, Younesian D, Eghbali P. Auxetic clamped-clamped resonators for high-efficiency vibration energy harvesting at low-frequency excitation. *Appl Energy* 2021;295:117010.
- [68] Eghbali P, Younesian D, Farhangdoust S. Enhancement of the low-frequency acoustic energy harvesting with auxetic resonators. *Appl Energy* 2020;270:115217.
- [69] Fang S, Du H, Yan T, Chen K, Li Z, Ma X, et al. Theoretical and experimental investigation on the advantages of auxetic nonlinear vortex-induced vibration energy harvesting. *Appl Energy* 2024;356:122395.
- [70] Gao Q, Lu Y, Shi Y, Liao WH, Yin G, Li J, et al. Enhancing the output performance of energy harvesters using hierarchical auxetic structure and optimization techniques. *IEEE Trans Ind Electron* 2024;71:11641–9.
- [71] Kabirian Z, Ebrahimian F, Younesian D, Eghbali P. Inlay-inspired meta-piezoelectric plates for the low-frequency vibration energy harvesting. *J Mater Sci Mater Electron* 2022;33:2909–20.
- [72] Roy Chowdhury A, Saurabh N, Kiran R, Patel S. Effect of porous auxetic structures on low-frequency piezoelectric energy harvesting systems: a finite element study. *Appl Phys A* 2021;128:62.
- [73] Chen K, Fang S, Gao Q, Zou D, Cao J, Liao WH. Enhancing power output of piezoelectric energy harvesting by gradient auxetic structures. *Appl Phys Lett* 2022;120:103901.
- [74] Plewa J, Płońska M, Junak G. Studies of auxetic structures assembled from rotating rectangles. *Materials* 2024;17:731.
- [75] Grima-Cornish JN, Attard D, Grima JN, Evans KE. Auxetic behavior and other negative thermomechanical properties from rotating rigid units. *Phys Status Solidi RRL Rapid Res Lett* 2021;16:2100322.
- [76] Grima JN, Evans KE. Auxetic behavior from rotating triangles. *J Mater Sci* 2006;41: 3193–6.
- [77] Grima JN, Chetcuti E, Manicaro E, Attard D, Camilleri M, Gatt R, et al. On the auxetic properties of generic rotating rigid triangles. *Proc R Soc A Math Phys Eng Sci* 2011;468:810–30.
- [78] Min Z, Chen Y, Shan X, Xie T. A novel double-arch piezoelectric energy harvester for capturing railway track vibration energy. *Energy* 2024;312:133636.
- [79] Chen K, Fang S, Gao Q, Zou D, Cao J, Liao WH. An enhanced nonlinear piezoelectric energy harvester with multiple rotating square unit cells. *Mech Syst Signal Process* 2022;173:109065.
- [80] Sui G, Shan X, Zhou C, Li H, Cheng T. Enhancing output performance of piezoelectric nanogenerator via negative Poisson's ratio effect. *Nano Energy* 2024; 130:110071.
- [81] Fang S, Chen K, Lai Z, Zhou S, Liao WH. Snap-through energy harvester with buckled mechanism and hierarchical auxetic structures for ultra-low-frequency rotational excitations. *Appl Phys Lett* 2023;122:093901.